Journal of Colloid and Interface Science 628 (2022) 435–445

Contents lists available at ScienceDirect

Journal of Colloid and Interface Science

journal homepage: www.elsevier.com/locate/jcis

Propulsion, deformation, and confinement response of hollow nanocellulose millimotors

Maryam Hosseini [a], Firoozeh Babayekhorasani [a], Ziyi Guo [a], Kang Liang [a], Vicki Chen [b], Patrick T. Spicer [a,*]

[a] School of Chemical Engineering, University of New South Wales, Sydney, NSW, Australia
[b] School of Chemical Engineering, University of Queensland, Queensland 4072, Australia

GRAPHICAL ABSTRACT

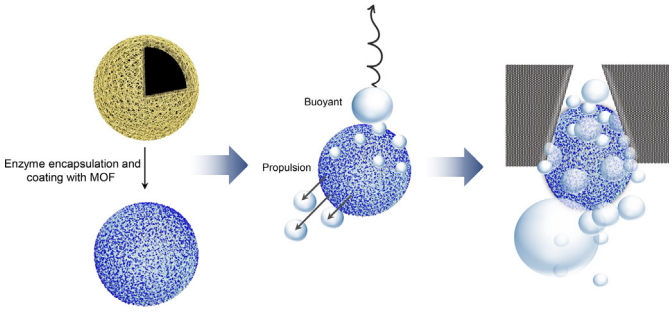

ARTICLE INFO

Article history:
Received 12 May 2022
Revised 26 July 2022
Accepted 5 August 2022
Available online 10 August 2022

2000 MSC:
2022
2000

Keywords:
Active matter
Nanocellulose
MOF
Enzyme

ABSTRACT

Hypothesis: Micromotor and nanomotor particles are typically made using dense solid particles that can sediment or be trapped in confined flow environments. Creation of much larger motors should be possible if a very low-density system is used with sufficient strength to carry liquid and still experience propulsive motion. Light, dense millimotors should also be able to deform more than dense solid ones in constrictions.

Experiments: Millimotors are created from permeable capsules of bacterial cellulose that are coated with catalse-containing metal–organic frameworks, enabling reactive propulsion in aqueous hydrogen peroxide. The motion of the motors is quantified using particle tracking and the deformation is measured using microcapillary compression and flow through confined channels.

Findings: Two different propulsion mechanisms are dominant depending on the motor surface chemistry: oxygen bubbles are expelled from hydrophilic millimotors, driving motion via recoil force and buoyancy. Hydrophobic millimotors remain attached to growing bubbles and move by buoyancy alone. Despite their large size, the low-density capsules compress to pass through contractions that would impede and be blocked by solid motors. The sparse structure but relatively large size of the motors enables them to transport significant volumes of liquid using minimal solid mass as a motor support structure.

* Corresponding author.
E-mail address: p.spicer@unsw.edu.au (P.T. Spicer).

https://doi.org/10.1016/j.jcis.2022.08.035
0021-9797/

List of Abbreviations

CAT	Catalase
CLSM	dynamic light scattering
DMSO	Dimethyl sulphoxide
FTIR	Fourier transform infrared
MOF	Metal–organic framework
NA	Numerical aperture
RhB	Rhodamine B isothiocyanate
SEM	Scanning electron microscope
XRD	X-ray Powder Diffraction
ZIF90	Zinc imidazolate-2-carboxyaldehyde
ZIFL	Zinc 2-methylimidazole

1. Introduction

Microorganisms can propel themselves through liquid by different swimming mechanisms, and synthetic particle motors, termed ‘‘active matter”, have been created that mimic microbial motion by chemical, rather than mechanical, means [1–3]. Particulate nanomotors and micromotors move by converting chemical fuel from their environment into kinetic energy, and can achieve remarkable speeds relative to their body length [4,5]. Propulsion can be driven by self-generated solute gradients or electric fields [1] or by formation of gas bubbles that cause buoyancy or ejection-induced recoil effects [6]. Applications for the small motors are imagined in drug delivery [7–9,2], environmental remediation [10–14], and self-assembly [15,16] while the particles' unique motion is widely studied as well [17]. Larger, millimeter-scale motors have recently been developed from clay/DNA membranes to act as synthetic protocells that move and carry out internal biochemical reactions [18]. These larger-scale motors can broaden the possible applications of active matter, motivating us to develop a millimotor capsule that is easily functionalized but can also overcome difficulties most motors face with confined space navigation and sedimentation potential [19].

Our approach to develop these new millimotors takes inspiration from the biological cells that active matter seeks to mimic. Cells are partially permeable to water, minimizing density differences, while their softness enables them to deform and pass through narrow spaces and navigate confined environments. By contrast, most synthetic active particles are made using dense solid materials, like platinum or silica, whose large density differences with water promote sedimentation. Such particles are also too rigid to deform and escape environmental confinement [19]. A recent review [20] identified low density and robust deformability as important goals for future motor particles, and this work focuses on a new approach to meeting these challenges using unconventionally large motor capsules made from a mesh of bacterial cellulose fibers.

Hollow capsules are a promising way to minimise mass use and density issues in motor particles [21–25] and their low density makes them behave like much smaller particles in fluid [26]. A recently developed bacterial cellulose capsule [27] provides a unique minimalist scaffolding for millimotor particle development, and we explore their motion and response after coating them with two different MOF nanoparticles [28]. The MOFs attach onto the capsule's cellulose nanofibers [29–31] and trap catalase enzyme in their structure [2,31], enabling conversion of aqueous hydrogen peroxide fuel into oxygen bubbles to drive motion [18,32]. The MOF surface polarity determines the mode of millimotor propulsion by altering oxygen bubble affinity for the capsule surface. The velocity and motion of the driven capsules are measured by optical microscopy and shown to be quite efficient compared to solid micro- and nanomotors, despite being much larger and full of liquid. The low-density shells are efficient motor bases because of their structural integrity and minimal mass, but also provide unique benefits for bubble-driven flow. The flexible nanocellulose fiber struts allow significant deformation when passing through constrictions and the permeable capsules form a low-friction gas layer on their surface that further enhances escape from confined spaces.

2. Methods and Materials

Cellulose capsule preparation: Cellulose capsules were synthesized by a biointerfacial polymerization process we previously developed [27]. Bacterial cellulose capsules were grown using a water-in-oil emulsion of bacterial culture droplets as templates. No surfactants are used as they would harm the cellulose-producing bacteria. Instead, the aqueous drops of bacterial culture are suspended in oil with a yield stress of $\sim$ 10 Pa as a result of crystallized hydrogenated castor oil wax. The yield stress keeps the droplets suspended and stable against coalescence [27]. The bacteria partition at droplet interfaces to access nutrients and oxygen, producing cellulose there that gradually becomes strongly entangled and can't move away from the interface once growth is complete.

The bacterial culture contains purified *Acetobacter xylinum* concentrated from Kombucha culture (Nourishme Organics, Australia) by gradient centrifugation, coconut water (Cocobella, Indonesia), and 10% w/v table sugar. Within 10 days, the encapsulated bacteria polymerize glucose molecules into cellulose nanofibers, with a diameter of 60–70 nm, that entangle to form a fiber mesh shell with a total thickness of 20–50 μm and a pore size of 0.5 μm [27] at the oil–water interface. Subsequently, catalase-ZIFL and catalase-ZIF90 MOF crystals were grown *in situ* on the nanofibers, producing hydrophobic and hydrophilic millimotors, respectively. Capsules ranged between 0.2–0.8 mm in diameter for both hydrophilic and hydrophobic particles.

Hydrophobic ZIFL coating: 5 g of catalase from bovine liver, (Sigma Aldrich), 200 μL of 14.8 mM zinc nitrate ($ZnNO_3$, Sigma Aldrich) aqueous solution and 2 mL of 714 mM 2-methylimidazole (Sigma Aldrich) aqueous solution were added to 1 mL of cellulose capsule dispersion. The mixture was mixed for 1 h and then rinsed several times with deionized water.

Hydrophilic ZIF90 coating: 5 g of catalase, 2 mL of 40 mM zinc nitrate ($ZnNO_3$, Sigma Aldrich) aqueous solution and 2 mL of 160 mM imidazolate-2-carboxyaldehyde (Sigma Aldrich) aqueous solution were added to 1 mL of cellulose capsule dispersion. The mixture was mixed for 1 h and rinsed with deionized water several times, Fig. 1.

Enzyme labelling: 8.5 mg of Rhodamine B isothiocyanate (RhB, Sigma Aldrich) was dissolved in 0.5 mL dimethyl sulphoxide (DMSO, Sigma Aldrich). In a glass vial, 40 mg of catalase was placed in 2 mL of sodium carbonate bicarbonate buffer (0.5 M, pH 9.5). Then, the RhB solution was added slowly into CAT solution. The CAT-RhB was then mixed for 2 h at room temperature in darkness. The unreacted enzymes were separated from the labelled enzymes in an Illustra NAP-25 column (GE Healthcare). The first band eluted

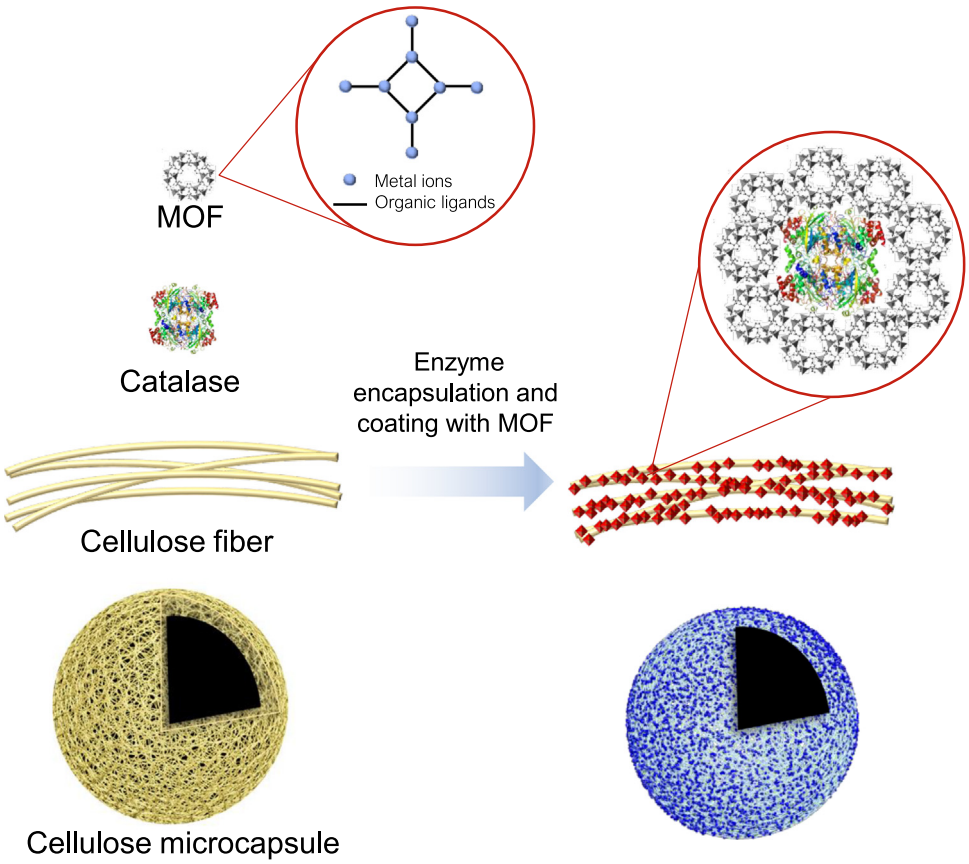

Fig. 1. Schematic illustration of the components of the millimotors and the process for coating the bacterial cellulose capsule with MOFs that contain catalase. The MOFs exist in the form of crystalline nanoparticles with a cage-like structure made of metal ions connected via organic ligands. Each crystal can encapsulate one or multiple biomolecules by physical adsorption [38–40]. The *in situ* growth of MOF crystals on cellulose fibers occurs by adsorption of the positively charged metal ions onto the cellulose hydroxyl group through electrostatic interaction. Subsequent addition of organic ligands enables co-precipitation with the metal ions to form MOF crystals on the fibers [31].

with Milli-Q water, which contains labeled enzymes, was collected for sample preparation.

MOF and cellulose labelling: Congo Red and FITC were used to stain cellulose fibers and MOF crystals, respectively, for visualization by addition of 34 mg of 0.5 wt% aqueous Congo Red solution to 1 mL of a cellulose capsule dispersion. The MOF is labeled with FITC using an existing procedure to covalently conjugate FITC to the organic ligands of the MOF [33,34]. Here 8 mg of FITC is dissolved in 2.5 mL of DMSO then added to the MOF solution. Sequentially the cellulose is first labeled with Congo Red, then MOFs with FITC. All samples incubated with FITC were kept dark and covered with aluminum foil to avoid photobleaching prior to confocal imaging.

Microscopy: Confocal and light sheet microscopy imaging experiments were carried out on a Zeiss LSM 880 with Airy scan [35], and Zeiss Lightsheet Z.1 (Germany) microscope. A 63x oil immersion objective, with numerical aperture NA = 1.4, 5x dry objective with NA = 0.16, and 20x water immersion objective with NA = 1 were used depending on the scale of observation desired. Low-magnification optical microscopy images were acquired via stereoscope (WILD M3C, Leica, Germany) with 6.4x objective to enable individual particle tracking in capsule dispersions at room temperature. ImageJ software was utilized to quantify the fluorescence intensity inside and outside of the capsule [36]. Scanning electron microscope (SEM) images of the samples were taken on an FEI Nova Nano SEM 230 FE-SEM at an accelerating voltage of 5.0 kV.

Fourier transform infrared spectroscopy (FTIR): FTIR patterns were collected on a Bruker IFS66/S High End FT-NIR/IR Spectrometer from 400 cm^{-1} to 4000 cm^{-1}.

Capsule deformation: Micropipette manipulation was used to apply controlled deformation to individual capsules. A microcapillary with a right-angle bend held the capsule in place while a second blunt microcapillary with an outer diameter of 1 mm was moved toward the capsule at a constant speed using a syringe pump stepper motor (Aladdin, WPI). The process was imaged at 200 frames per second using an Opticam CMOS camera (Qimaging).

Dissolved oxygen: Dissolved oxygen measurements were performed using a dissolved oxygen meter (Oakton DO 6+) to quantify propulsion reaction kinetics for both hydrophobic (ZIFL) and hydrophilic (ZIF90) motors in the presence of 1% v/v H_2O_2.

3. Results and discussion

3.1. Capsule characterization

Cellulose capsules are created using aqueous emulsion droplets of *Acetobacter* bacteria culture as templates. The bacteria produce an entangled shell of cellulose fibers with micron-scale length and nanometer-scale thickness, Fig. 1. The overall capsule diameter is millimeter-sized like the emulsion droplet templates used to grow them [27]. While large capsules are easy to make, the lower size limit is set by the size of a small droplet of bacterial culture. Since bacteria are on the order of 3 μm long, the smallest capsules we can make tend to be several times larger $\sim$ 50 μm [27].

The use of the cellulose scaffolding provides a balance of structural integrity and flexibility with a signficant cargo volume. For example, a 0.5 mm diameter capsule with a 20 μm shell thickness

has a mass of only 200 ng because of its high porosity, but its internal volume holds 400,000 times more water mass. The capsules are modified to enable fuel-driven motion by attaching to the fibers a large number of active MOF nanoparticles that contain catalase enzyme in their pores [28]. The MOF particles created here are a crystalline matrix of zinc ions connected by two different organic ligands that allow us to produce motors coated with hydrophilic ZIF90 MOFs, using imidazolate-2-carboxyaldehyde ligand, and a version coated with hydrophobic ZIFL MOFs, using 2-methylimidazole ligands, Fig. 1. The 60 kDa catalase we used has a hydrodynamic diameter of ~ 7.4 nm and is encapsulated within the porous structure of the larger polycrystalline MOF nanoparticles that precipitate on the cellulose. The process of coating cellulose nanofibers with MOF particles is shown schematically in Fig. 1. First, positively charged zinc ions are adsorbed on the cellulose hydroxyl surface group. After adding organic ligands, micron-scale MOF particles crystallize on the 60 nm cellulose fibers, altering the capsule porosity and mechanical properties. The two MOF structures used have the same zinc metal ion basis but are connected by two different hydrophilic and hydrophobic ligands to vary the particles' surface chemistry and swimming behavior.

FTIR was used to assess the success of MOF and enzyme coating on the capsules by measuring the presence of the ligand and enzyme chemical groups, Fig. 2. For ZIFL, the characteristic peaks at 1585, 1147, ~750 (double bonds) and 423 cm^{-1} correspond to the stretching vibration of C = N, bending vibration of CH, bending vibration of the imidazole ring and vibration peak of Zn-N, respectively. The presence of these peaks indicates the significant presence of the 2-methylimidazole ligands in the ZIFL. The absorbance spectrum of ZIF90, shown in Fig. 2a), has a prominent mode centred at 1671 cm^{-1}, extending from 1751 to 1551 cm^{-1}, that is attributed to a C = O stretch [37] in the imidazolate-2-carboxyaldehyde ligand structure. The position and intensity of this carbonyl band obscures the amide I and, partially, the amide II spectral features of the catalase. Fig. 2(a) shows the amide II spectral region with two peaks centered at about 1540 and 1515 cm^{-1}. The position of these bands is consistent with the amide II components of free catalase, showing its successful encapsulation in the MOF particles on the cellulose fibers [24]. Despite the lower sensitivity of amide II to protein secondary structure versus amide I, we conclude that the secondary structure of catalase-ZIF90 is comparable to catalase-ZIFL [24]. Structural studies of the crystalline MOFs formed on the capsules showed identical diffraction patterns for both ZIFL and ZIF90 after enzyme encapsulation and attachment to the cellulose capsule, Figure S1.

Fig. 2(b) shows an SEM image of native cellulose nanofibers in a capsule. The original cellulose fibers in the pristine capsules are quite strong and thin, but the deposition of metallic MOF nanoparticle networks onto these fibers will modify them in a number of ways, including their mechanical properties and the overall capsule permeability to the fluid environment. The patterns of deposition will also affect the mode of propulsion by catalysis, so we characterize their state by imaging. Figs. 2(c-f) show crystals of ZIFL and ZIF90 deposits on the capsule fibers. The capsules were freeze-dried at −65°C to avoid any collapse that might occur by capillary pressure during air drying. As shown in Fig. 2, the fiber diameter is between 20–70 nm with a length of several microns for the unmodified cellulose capsule [27]. After precipitation of MOF on the capsules, particles with an average size of 100–150 nm for ZIFL and 150 nm for ZIF90 attached to the surface of the cellulose fibers, Fig. 2(c-d). The addition of the MOF particles to the capsule is expected to alter the mass and inertia of the system during subsequent propulsion studies. If we assume the MOF coating is a 99% dense single layer of 100 nm particles with a density of 2 g/cm^3, the particles add 150 ng mass to a 0.5 mm diameter cellulose capsule, at most doubling its weight while still being dominated by the mass of the liquid cargo in its capsule.

Differences can be seen in the coating morphology at higher magnifications, Fig. 2(e-f), based on the polarity of the MOF particles produced. For example, the hydrophobic ZIFL particles form structures that partially span the gaps between fibers Fig. 2(e), likely because the particles have affinity for the cellulose. The hydrophilic ZIF90 coatings seem to follow the fiber structures less closely due to less intimate contact, Fig. 2(f). Although different morpholgies form on the capsules, MOF film growth on individual fibers increases the effective fiber size and reduce the pore size of the overall capsule. Previous measurements [27] indicated the pristine capsules have pore sizes on the order of 500 nm so the

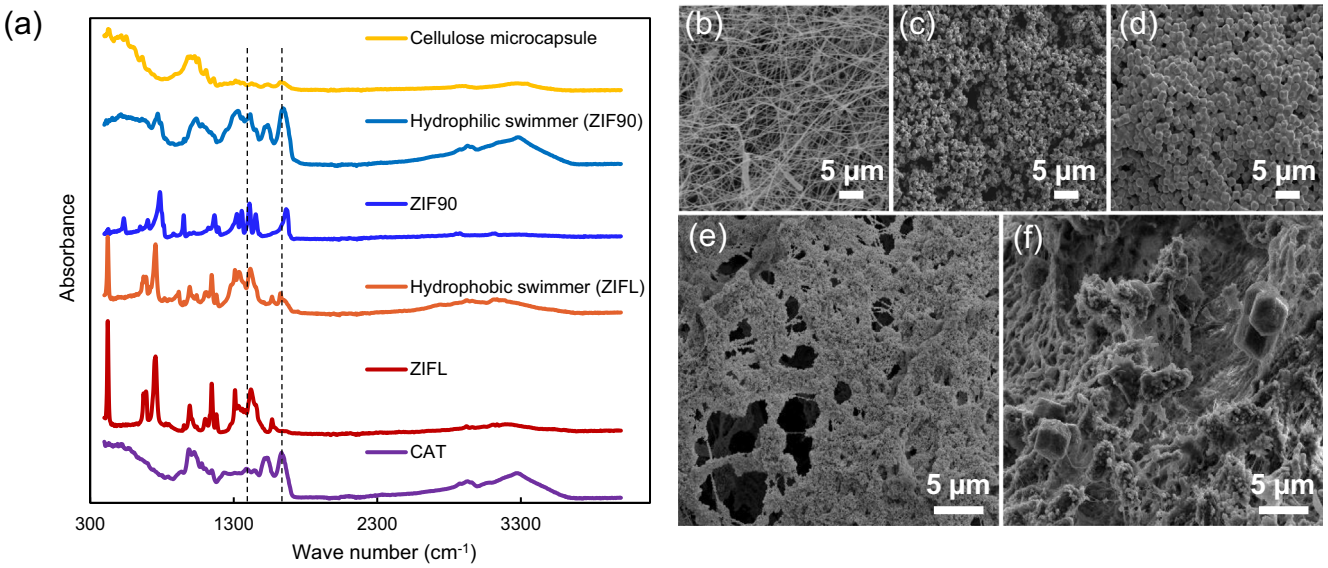

Fig. 2. (a) FTIR spectra of pure catalase (CAT), both MOF types, pristine cellulose capsules, and cellulose capsules after MOF coating. IR peaks show successful combination of enzyme, MOF, and cellulose fibers. (b) SEM of pristine cellulose capsule surfaces, (c) hydrophilic ZIF90 MOF particles, (d) hydrophobic ZIFL MOF particles. (e and f) Higher magnification views of cellulose fibers coated with MOF particles, highlighting the reinforcement of the cellulose capsule fibers by the dense deposits as well as some reduction in pore size. The MOF particle coatings on cellulose fibers tend to form pore-spanning bridges for (e) hydrophobic ZIFL MOF while deposits tend to follow the fiber structure more for (f) hydrophilic ZIF90 MOF. All scale bars 5 μm.

MOF crystals will rapidly reduce the overall capsule permeability as they grow.

Different microscopy techniques were used to visualize the pristine and modified cellulose capsule at larger length scales for a more holistic characterization. Light sheet fluorescence microscopy (LSFM) allows us to visualize the full 3D structure of the millimotors. Cellulose, MOFs, and catalase were stained with Congo Red, FITC, and Rhodamine B, respectively, before fluorescent imaging. Figs. 3(a-c) show 3D reconstructions of pristine and modified cellulose capsules coated by both MOF types, with the cellulose fibers shown in red. At this magnification, the pristine capsule in Fig. 3(a) looks spherical and almost solid as the capsule pores are micron-scale [27]. A capsule with the hydrophilic ZIF90 MOF coating is shown in Fig. 3b) and the impact of the MOF coating is clearest in the dark regions of the spherical capsule where larger MOF regions obscure the cellulose fibers. The coating is heterogeneous due to random variations in the solution during precipitation. More detail can be resolved at higher magnifications.

Higher resolution imaging is performed using confocal microscopy to visualize the hollow and fibrous structure of the capsules, with and without a MOF coating, Figs. 3(d-i). Figs. 3(d-f) show a single mid-plane slice through the capsule, demonstrating that the capsules are largely hollow, and have a shell on the order of 20 μm in agreement with past work [27]. The capsules with hydrophilic ZIF90 and hydrophobic ZIFL MOF coatings in Fig. 3(e-f) have similar shell thicknesses to the pristine capsule in Fig. 3(d), as the nanoscale MOF coatings coat individual fibers and don't significantly change the overall wall thickness. An even higher magnification view of the capsule shells highlights the degree of penetration of the fiber structures by the MOF particles being deposited, Figs. 3(g-i). Here the MOF nanoparticles are shown as yellow and the cellulose fibers as red. The optical resolution of the confocal

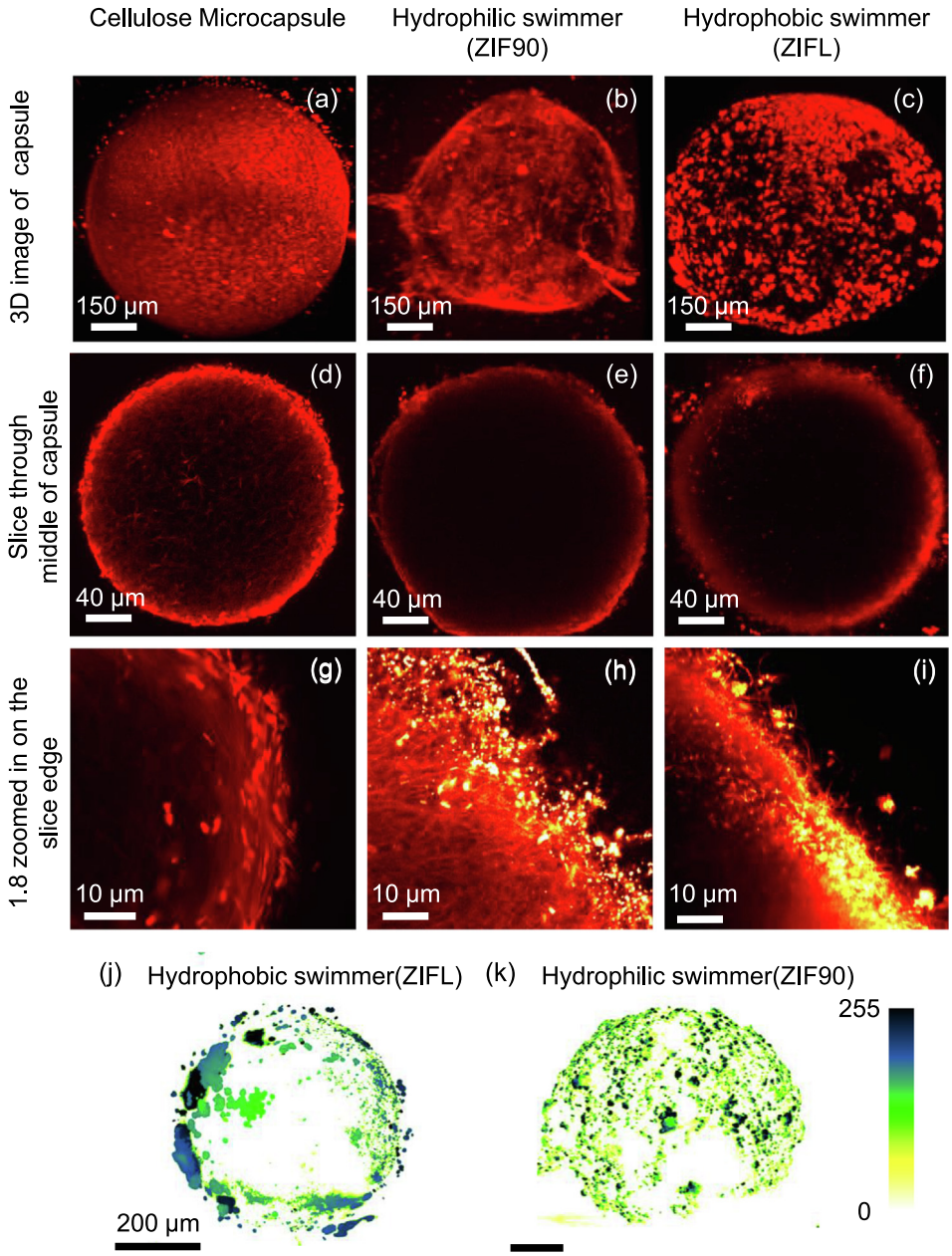

Fig. 3. Lightsheet fluorescence microscopy shows 3D reconstructions of the (a) pristine cellulose capsule, (b) a capsule coated with hydrophilic ZIF90, and (c) hydrophobic ZIFL MOFs. A single mid-plane slice through the capsule (d) before and after coating with (e) hydrophilic and (f) hydrophobic MOF. (h-i) Higher magnification confocal images show MOF particles in yellow and cellulose fibers in red. 3D images of enzyme distribution on the (j) hydrophobic and (k) hydrophilic millimotor surface.

system used here is on the order of 200 nm so these images will not resolve the smallest deposits formed and only indicate the degree of individual fiber coating by the MOFs. As the MOF particles are the framework we use to encapsulate the catalase enzyme for propulsion, the distribution of both is of interest to particle design and motor performance.

Enzyme distribution is a key parameter determining millimotor motion and orientation [41]. The distribution of enzyme on the MOF-coated capsules is demonstrated in Figs. 3(j-k) using a 3D reconstruction of the millimotor capsules with a color map indicating the intensity of the Rhodamine B dye labeling the catalase. We observe a heterogeneous but thorough distribution of the enzyme on the surface of the hydrophobic motor, Fig. 3(j), but an asymmetric distribution along the top half of the surface of the hydrophilic millimotor, possibly because of a higher affinity of the enzyme for the hydrophobic MOFs, causing some segregation on the hydrophilic system [42]. A bulk-scale measurement of enzyme availability, a Bradford assay [43], was also used to calculate the encapsulation efficiency of catalase as 98.2% for hydrophobic ZIFL and 85.9% in hydrophilic ZIF90 motors. The difference in spatial distribution of the enzyme on the capsules could potentially affect self-propulsion of the motors by inhomogeneous oxygen bubble production [41,44] but for buoyancy-dominated motion such an effect should be negligible. The MOF coatings on the capsules can also affect porosity of the capsules, so we now assess modified capsule exchange with the fluid environment.

3.2. Porosity of motors

Song et al. [27] studied the permeability of pristine cellulose capsules and found a pore size on the order of 500 nm. After surface modification of the capsules by MOF deposition, Fig. 3, we expect the pore size to change significantly so we study this by molecular tracer diffusion experiments. FITC-labeled dextran chains ranging from 4–40 kDa were used as tracers to determine the permeability of MOF-coated cellulose capsules based on size exclusion. After mixing capsules with 1 mg/ml of FITC-dextran and 24 h incubation, confocal microscopy images of capsules were obtained to determine the ability of different sizes to penetrate the coated capsules. Figs. 4(a-c) show capsules that have been exposed to different size FITC-dextrans and the intensity of green tracer that was able to diffuse inside of the capsules coated with hydrophilic ZIF90 provides a measure of the new capsule pore size. The 4 and 19 kDa tracers penetrate the hydrophilic ZIF90 capsules in Figs. 4(a-b), indicating a pore size larger than 1.9 nm, while the 40 kDa remains outside of the capsule, Fig. 4(c), blocked by the new pore size and indicating the hydrophilic capsule is impermeable to 4.3 nm species [45]. Ten different sets of capsules were tested for reproducibility and the same results were obtained as above.

For hydrophobic ZIFL coated capsules, 4 kDa FITC-dextran shows a small amount of diffusion inside the capsule after 24 h. However, 19 and 40 kDa molecular weight FITC-dextran chains

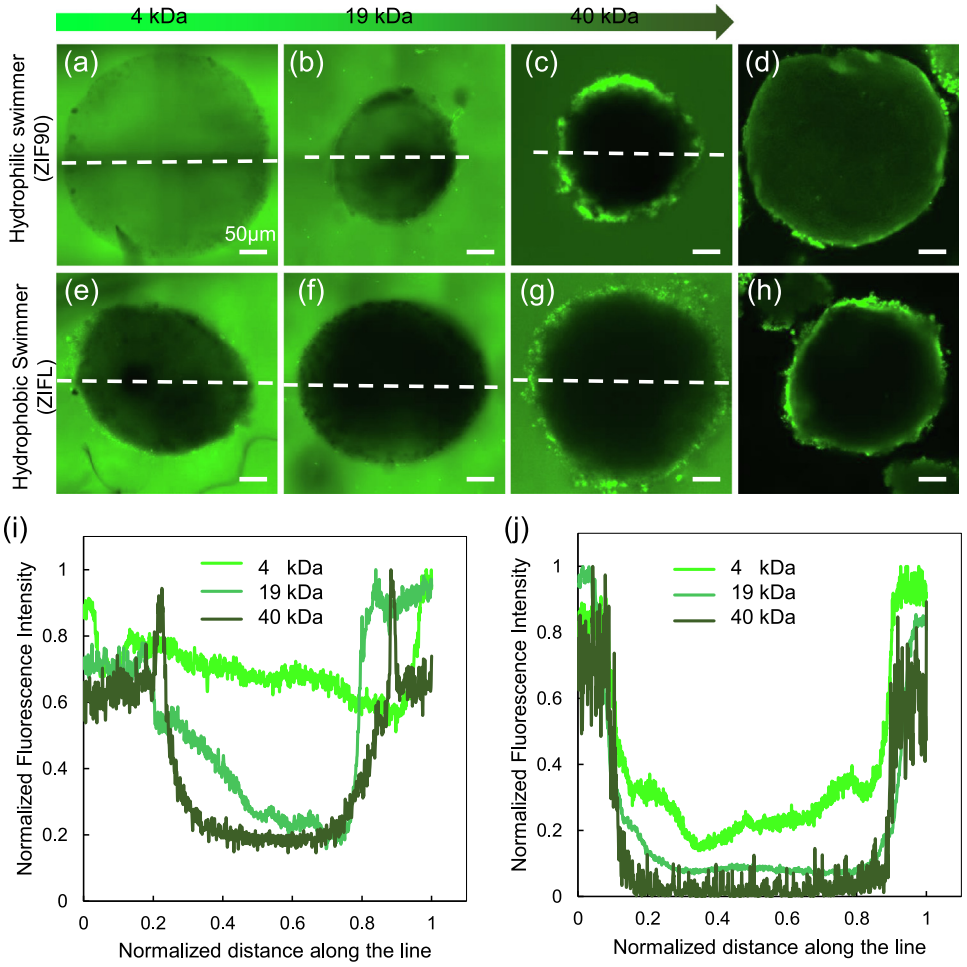

Fig. 4. Measurement of permeability of (a-c) hydrophilic and (e-g) hydrophobic millimotors based on transport of three different FITC-dextran tracers with molecular weight ranging from 4–40 kDa. Figures (d) and (h) show capsules that contained 40 kDa dextran before being coated with MOFs to demonstrate their encapsulation ability. The FITC-dextran concentration varies from green regions of high concentrations to black where no FITC-dextran is resolved. Scale bars are 50 μm. The fluorescence intensity in (a-g) is summarized by plotting integrated normalized intensity of the images for the (i) hydrophilic ZIF90 and (j) hydrophobic millimotors.

are totally excluded. These capsule pores must then have an average diameter less than 1.9 nm [45]. A second experiment was performed to confirm the upper limit of pore size of both capsule types: we immersed capsules in 40 kDa FITC-dextran and *then* coated them with hydrophilic and hydrophobic MOFs. After washing the capsules with deionized water multiple times, and holding for 24 h, we saw no release of FITC-dextran from either hydrophilic or hydrophobic capsules, Figs. 4(d) and (h), respectively. Different reaction times and conditions could alter these effects, but the results in Fig. 4 indicate a more than 100X variation in pore size, from 500 nm to 4 nm, is possible for MOF-coated cellulose capsules. For comparison, plant cells have a cellulose structure that is permeable to molecules with a diameter ranging from 3.5–5.2 nm [46]. MOF coating of capsule fibers enables us to create motors with chemical propulsion as well as tunable permeability and solute exchange.

Because the dextran is shown to be uniformly blocked by the coating, it indicates a fairly uniform coating, on average, by the MOFs given the deposition occurs throughout the thickness of the capsule walls. So the capsules remain permeable after coating, though much less so than their more permeable pristine form, meaning they can fill with fluid and carry that cargo during movement. It also means the coated capsule millimotors can still exchange contents with the environment via molecular diffusion, for example to perform delivery of a chemical cargo [18]. The length scale of the pores can then be used to control the subsequent selectivity of the capsule in these applications.

3.3. Millimotor capsule propulsion

Oxygen gas production and bubble formation play an essential role in propulsion of both hydrophobic and hydrophilic millimotors. When exposed to an aqueous hydrogen peroxide solution, catalase enzyme immobilized in the MOFs catalyzes hydrogen peroxide decomposition into oxygen and water molecules, with the excess oxygen gas forming bubbles and driving motion. We first assess the rate of reactive oxygen generation [28,42,47] in a bulk solution of 1% v/v H_2O_2 containing hydrophobic ZIFL and hydrophilic ZIF90 motors, Fig. 5(a). Both systems rapidly produce oxygen, but the rate of O_2 production by hydrophilic ZIF90 motors was more than six times that by hydrophobic ZIFL motors, Fig. 5(a), as a result of differences in enzyme activity. The catalase enzyme has a higher affinity for a hydrophobic surface, which can cause conformation changes that denature the protein, reducing its activity [42]. Oxygen production rate is important to motor performance, as sufficiently high rates can lead to bubble ejection and propulsion by recoil forces, whereas slower growth tends to favor bubbles remaining attached to a motor so that motion is dominated by buoyancy. The mode of bubble-motor interaction, however, is also affected by the motor surface chemistry and the resultant affinity of hydrophobic bubbles for a motor.

We studied the performance of these motors by observation of an aqueous dispersion of individual or multiple enzyme-powered millimotors. The motors were placed in a transparent cuvette and allowed to sediment, then different concentrations of aqueous hydrogen peroxide solution ranging from 0.065–1% were added and allowed to diffuse to the motors at the bottom to initiate propulsion. Once peroxide decomposition began, cellulose millimotors became buoyant and migrated from a resting position at the bottom of the cuvette to the rest of the fluid volume. A high-speed camera was utilized to observe growth of single and multiple oxygen bubbles inside or outside of the motors in less than a minute after addition of hydrogen peroxide.

In all motion studies, we see a clear difference between the hydrophilic ZIF90 motors, that initially move in various directions as a result of rapid bubble production and ejection, and the hydrophobic ZIFL motors that only move vertically, Fig. 5(b). For example, the hydrophobic ZIFL motor in the top row of Fig. 5(b) follows a completely vertical trajectory over several seconds until it reaches the top of the water volume and drifts slightly to the side.

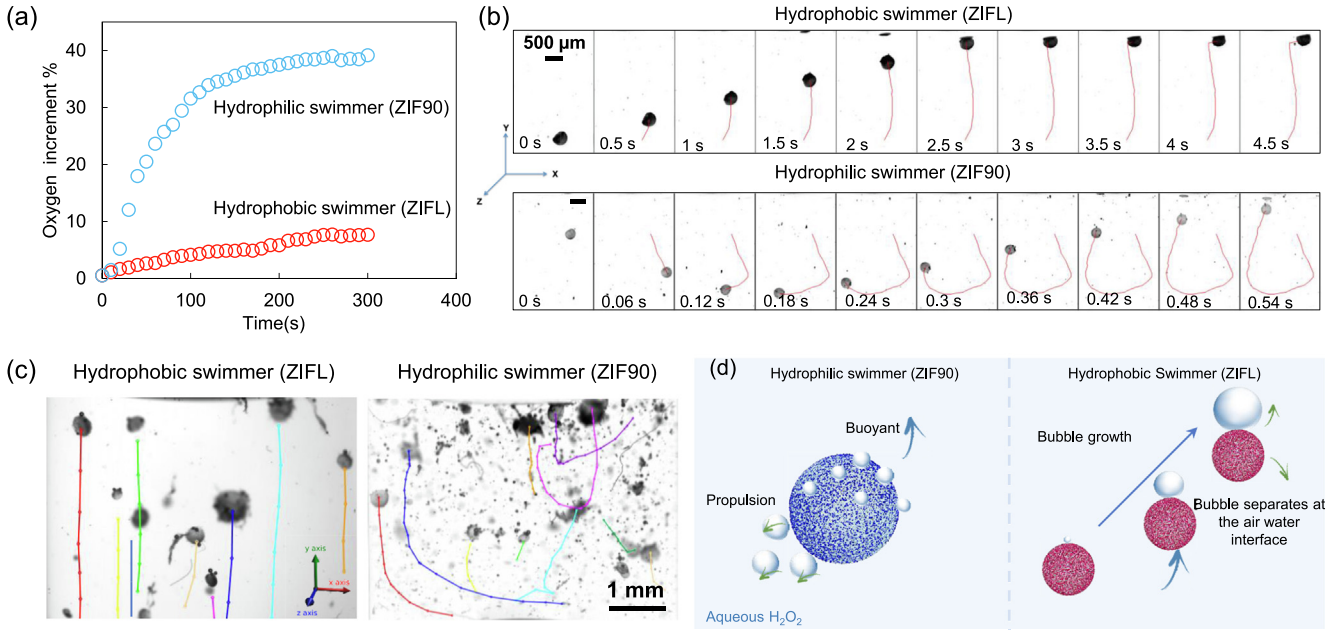

Fig. 5. (a) Oxygen gas increment measurements in an aqueous 1% hydrogen peroxide solution containing dispersed hydrophilic or hydrophobic millimotors. (b) Time-lapse images of hydrophobic ZIFL (first row) and hydrophilic ZIF90 (second row) motor trajectories in aqueous 0.25 wt% H_2O_2. For hydrophobic motors, higher MOF deposition makes the motors denser so they sediment to the bottom. Bubble formation and growth then lifts motors vertically via buoyancy. For hydrophilic motors, both bubble propulsion and buoyancy contribute to motion, initially driving motors in erratic directions then mostly vertically. (c) Multiple hydrophilic and hydrophobic motors have similar traits, moving vertically when buoyancy dominates and in multiple directions when both buoyancy and propulsive recoil contribute. (d) Schematic of the proposed mechanism for millimotor bubble formation and movement: hydrophobic motors remain attached to O_2 bubbles and their motion is dominated by buoyancy, while hydrophilic motors have elements of horizontal motion due to propulsion by bubble ejection as well as buoyancy.

This is consistent with extensive work on mineral flotation, where hydrophobic particles are separated from suspensions using air bubbles that flow through the system [48,49]. The hydrophilic ZIF90 motor in the bottom row of Fig. 5(b), however, initially moves down as a result of ejecting a bubble upward, then makes a hard turn to our left and moves across the bottom of the cuvette. After these two major direction changes, the motor then moves up as buoyancy becomes dominant. Multiple millimotors in dispersion behave similarly, as shown in Fig. 5(c) for a 0.05 wt% solution of hydrogen peroxide. The hydrophobic ZIFL motors all follow remarkably consistent vertical trajectories as their motion is dominated by buoyancy due to growth of strongly attached bubbles, Figure S2. The hydrophilic ZIF90 motors, however, show more complex motion that can lead to correlated trajectories, like the two motors in the bottom left corner of the image, but opposing directions are also possible as seen in the upper right region of the image. The enzymatic activity is maintained until the exhaustion of the chemical fuel, so adjusting the concentration increases the initial rates of movement and extends the length of time that movement can be observed. The two motor surface chemistries thus enable different directions of movement. Bubbles can be generated wherever enzymes are located on the surface of the motors, so if the bubble is initially ejected the motor will move in the opposite direction by recoil. If bubbles remain attached, however, the motor will move up by buoyancy and its initial orientation is less significant to the subsequent motion. We summarize the mechanisms of motion by schematic in Fig. 5(d).

The cellulose capsules used here vary in size from 200–600 μm, all much larger than commonly-studied micro- and nanomotors, but consistent with recently-developed protocell millimotors [18]. We are curious about the performance of these motors versus their smaller counterparts, however, as their large size but low solid mass could provide additional benefits. As noted earlier, the capsules are low-density and permeable, with the majority of their inertia due to water that permeates the interior. A useful benchmark is the motor velocity relative to its diameter, where impressive values of 4–200 diameters/s are known [4]. Here we see hydrophobic ZIFL millimotors regularly moving at average velocities of up to 4 mm/s, with a standard error of 0.6 mm/s. This represents a relative velocity of more than 8 diameters/s. Hydrophilic ZIF90 millimotors can reach average velocities of 40 mm/s, with a standard error of 14 mm/s, Figure S3. This represents a relative velocity of more than 80 diameters/s. The difference is the result of the recoil force exhibited by only the hydrophilic ZIF90 motors, as buoyancy is the only other mechanism possible for both systems. Given that these motors are orders of magnitude larger than micro- or nanomotors, it is encouraging to note their propulsion, even while containing a massive liquid cargo, is competitive with the much smaller solid motors.

3.4. Motor deformation and confinement response

The cellulose motors have a unique porosity and response to mechanical stress because of their combined strength and flexibility [27]. As a result, we are interested in how these particles affect capsule response to extensional stress. First, we need to evaluate the extent to which the modification of the motors by the formation of MOF crystals affects their mechanical properties. Song et al. [27] found unmodified capsules deformed elastically under compression, recovering after deformations as large as 20% but remaining indented or buckled at higher strains. Adding crystalline MOF particles, however, is expected to stiffen the fibers and change the capsule response to deformation. Stress–strain curves for up to five individual millimotors, Figure S4, were measured using an extensional flow in a microfluidic channel [27]. We found that the elastic modulus, E = 100 Pa, of pristine cellulose capsules increased $\sim 30X$ after coating with hydrophilic ZIF90 MOFs and $\sim 140X$ after coating with hydrophobic ZIFL MOFs. The difference is likely a result of variations in coating uniformity and distribution, Fig. 2. Because of the small sample size we have available for testing, the mechanical measurements can not be taken to be fully representative of all our particles and are indicative only of the likely magnitude of the capsule moduli.

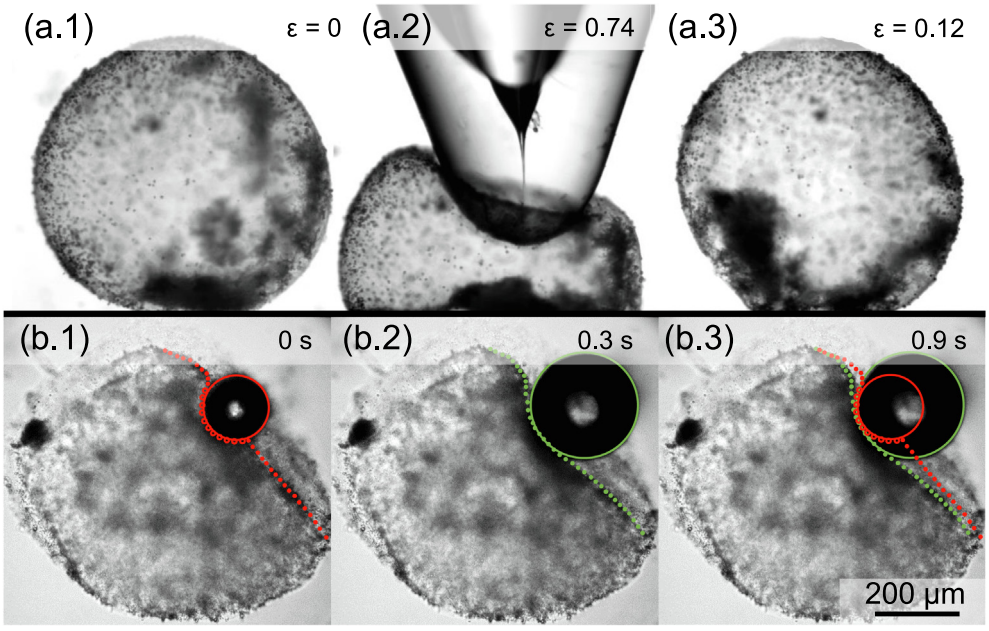

Fig. 6. Deformation and recovery of hydrophobic (a1-a3) motors using microcapillary manipulation. The capsule was deformed by a capillary tip, and each column indicates the stage of initial, deformation, and recovery. The spherical shape of the hydrophobic motor is recovered after 75% strain. (b1-b3) Successive images show the growth of an oxygen bubble on the surface of a hydrophobic ZIFL capsule over 5 ms intervals. The capsule deforms under the stress exerted by the bubble, indicating an ability to change shape during movement as the drawn lines document.

Along with an increased elastic modulus, the capsules preserve significant ability to recover from deformation, as we demonstrate in Fig. 6. Fig. 6(a) shows the microscopic response of a hydrophobic ZIFL millimotor to deformation by a blunt microcapillary end. Both hydrophobic ZIFL and hydrophilic ZIF90 motors largely recover their original profile after being indented by external stress to a strain of ε = 74% and higher, while pristine capsules do not fully recover from strains higher than ε = 20% [27]. The addition of MOFs clearly increases the elasticity of the capsules while adding propulsive capability. This is consistent with above estimates of a significantly increased capsule modulus after MOF coating.

Fig. 6(b) suggests an even more interesting dimension to the flexibility of these motors. A series of successive close-up images of a bubble evolving on a hydrophobic ZIFL motor surface in Fig. 6(b) indicates that the motor structure actually flexes in response to the pressure of the bubble expansion itself. Here the bubble is likely generated inside of the capsule and then squeezes out of a pore to exert the pressure seen here. Such an effect could also occur if the bubble formed on a capsule that was confined in some way. The result indicates the motors could actually be changing shape during motion, increasing their flexibility and responsiveness, and offering a mechanism for more complex movements in future work. As pointed out earlier, there is a need for motors to navigate confined environments while adapting and recovering to the different conditions they encounter. We now evaluate whether such deformation and response can occur when the millimotors encounter confinement during their propelled movement. We do this by studying the performance of the motors during propulsion in a constricted channel and note whether the combination of propulsion and flexibility enhance their mobility.

Fig. 7(a) shows a series of images of a hydrophilic ZIF90 motor as it moves vertically through a gradually constricting capillary. Here, to enhance visibility of the position of the motor in the image frames, we have false colored the motor red, water blue, and the glass capillary gray. The spherical millimotor initially has a diameter of 2.9 mm so can enter the capillary but must compress in order to exit, as the capillary internal diameter reduces from 3.5 mm to 2.2 mm at its outlet. The motor is initially driven by buoyancy but slows in the second frame in response to the narrowed passage. The narrowing of the channel causes compression of the motor, increasing its strain to more than 25%, Fig. 7(c). However, the motor continues to produce bubbles behind itself that grow as the reaction proceeds. A solid particle at this point would be unable to proceed and simply block the channel, but the flexible motor is able to deform much more in response to stress, Fig. 6(a), and continues to move, albeit in a more cyclical way as seen in the plot of vertical position in Fig. 7(b). Despite the small variations in velocity, the overall progress of the motor is relatively constant as a result of its flexibility and reactive propulsion. The growth of surface bubbles likely aids movement by reducing drag on the capsule. Fig. 7(a) also shows the formation of a large bubble behind the motor that aids in pushing it through the constriction. Interestingly, the bubble driving the capsules through the capillary is pinned to the capillary wall, allowing it to push against the capsule. Such behavior is beneficial for this additional propulsion mechanism to act, as a non-wetting capillary surface would reduce the ability of the bubble to push the motor. The results in Fig. 7 show that the production of deformable responsive motors with the low-density cellulose capsules developed here enable use in confined environments that solid particle counterparts can not handle. A high level of deformation might be expected to cause erosion of

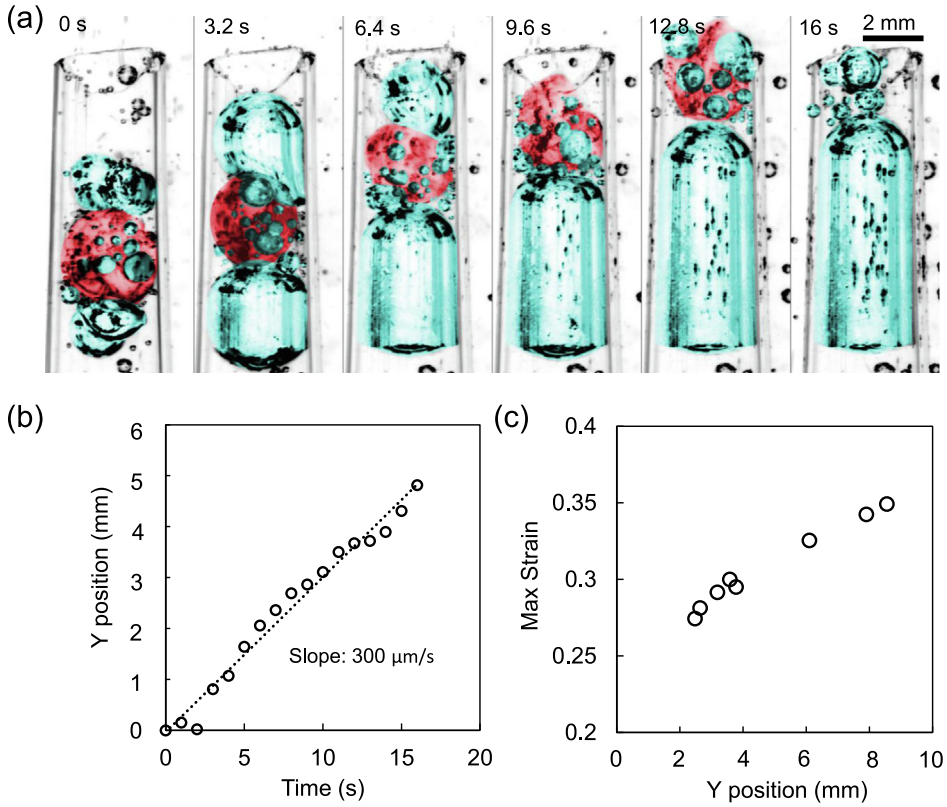

Fig. 7. (a) Composite images of the hydrophilic motor passing through a constriction in an aqueous solution of 3% H_2O_2. (b) The slope of the vertical position and time plot shows the velocity of the hydrophilic motor, around 300 μm/s, during its motion through the confined channel. (c) Changing hydrophilic motor strain at different vertical positions in the constriction.

the MOFs from the capsules surface; however, no detectable fragments or associated turbidity were observed following the deformation experiments in Fig. 6(a). In addition, the results in Fig. 7 indicate propulsion is maintained even during quite robust deformation in confinement, further confirming the motors largely remain attached.

4. Conclusions

In this study, enzyme-powered millimotors have been made by precipitation of MOF particles encapsulating catalase enzymes onto soft cellulose capsules. The large size, but low mass of the motors makes them a unique addition to the range of existing particle motors as they are able to carry significant volumes of liquid cargo because of their permeability. The large capsules are able to move using chemical fuel thanks to the numerous nanomotors attached to their surfaces, analogous to a large tanker ship driven by multiple tugboats.

Two mechanisms of propulsion result from enzyme-mediated production of oxygen gas bubbles in the presence of hydrogen peroxide. Bubbles grow on and remain attached to hydrophobic motors, driving vertical motion as buoyancy rapidly grows. For hydrophilic motors, bubbles are initially expelled from the structures, driving randomly-directed motion by recoil force, but as more bubbles grow motion becomes dominated by buoyancy and the motors rise similarly to the hydrophobic motors. Despite their large size, the millimotors move with surprising speeds, reaching levels of 80 motor diameters per second for the hydrophilic motors, when recoil force dominates movement, and 8 motor diameters per second when buoyancy dominates. The low density of the millimotors makes them highly efficient at movement, exhibiting similar or faster relative velocities than much smaller solid particle motors. The flexible response to mechanical stress of the millimotors enables them to squeeze through significant constrictions, making their mobility viable even in confined spaces and environments where solid motor particles would clog and jam. The millimotors can compress their diameter by as much as 30% in a constriction and their continuous generation of gas bubbles creates a low-slip surface layer and a back-pressure that enhances movement through tight spots. Such flexibility also offers a possible way to rapidly release the liquid cargo of the capsules and we plan to study this, and the movement of capsules through more complex porous media, in future work.

Declaration of Competing Interest

The authors declare that they have no known competing financial interests or personal relationships that could have appeared to influence the work reported in this paper.

Acknowledgement

MH acknowledges support from a UNSW Scientia PhD fellowship. The authors acknowledge partial support from the Australian Government through the Australian Research Council's Discovery Projects funding scheme, Project DP190102614. Lightsheet, confocal, and scanning electron microscopy were performed using instruments situated in, and maintained by, the Katharina Gaus Light Microscopy Facility (KGLMF) and Electron Microscope Unit (EMU) at the Mark Wainwright Analytical Centre, UNSW Sydney.

Appendix A. Supplementary material

Supplementary data associated with this article can be found, in the online version, at https://doi.org/10.1016/j.jcis.2022.08.035.

References

[1] J.L. Moran, J.D. Posner, Phoretic self-propulsion, Annu. Rev. Fluid Mech. 49 (2017) 511–540.
[2] E. Ma, K. Wang, Z. Hu, H. Wang, Dual-stimuli-responsive cus-based micromotors for efficient photo-fenton degradation of antibiotics, J. Colloid Interface Sci. 603 (2021) 685–694.
[3] Y. Tao, X. Li, Z. Wu, C. Chen, K. Tan, M. Wan, M. Zhou, C. Mao, Nitric oxide-driven nanomotors with bowl-shaped mesoporous silica for targeted thrombolysis, Journal of colloid and interface science 611 (2022) 61–70.
[4] W. Gao, S. Sattayasamitsathit, J. Wang, Catalytically propelled micro-/nanomotors: how fast can they move?, The Chemical Record 12 (1) (2012) 224–231
[5] M. Yan, L. Xie, J. Tang, K. Liang, Y. Mei, B. Kong, Recent advances in heterosilica-based micro/nanomotors: designs, biomedical applications, and future perspectives, Chem. Mater. 33 (9) (2021) 3022–3046.
[6] H. Wang, J.G.S. Moo, M. Pumera, From nanomotors to micromotors: The influence of the size of an autonomous bubble-propelled device upon its motion, ACS nano 10 (5) (2016) 5041–5050.
[7] S. Tang, F. Zhang, H. Gong, F. Wei, J. Zhuang, E. Karshalev, B.E.-F. de Ávila, C. Huang, Z. Zhou, Z. Li, et al., Enzyme-powered janus platelet cell robots for active and targeted drug delivery, Science Robotics 5 (43).
[8] B. Esteban-Fernández de Ávila, M.A. Lopez-Ramirez, R. Mundaca-Uribe, X. Wei, D.E. Ramírez-Herrera, E. Karshalev, B. Nguyen, R.H. Fang, L. Zhang, J. Wang, Multicompartment tubular micromotors toward enhanced localized active delivery, Adv. Mater. 32 (25) (2020) 2000091.
[9] S. Gao, J. Hou, J. Zeng, J.J. Richardson, Z. Gu, X. Gao, D. Li, M. Gao, D.-W. Wang, P. Chen, et al., Superassembled biocatalytic porous framework micromotors with reversible and sensitive ph-speed regulation at ultralow physiological h2o2 concentration, Adv. Funct. Mater. 29 (18) (2019) 1808900.
[10] M. Zarei, M. Zarei, Self-propelled micro/nanomotors for sensing and environmental remediation, Small 14 (30) (2018) 1800912.
[11] B. Qiu, L. Xie, J. Zeng, T. Liu, M. Yan, S. Zhou, Q. Liang, J. Tang, K. Liang, B. Kong, Interfacially super-assembled asymmetric and h2o2 sensitive multilayer-sandwich magnetic mesoporous silica nanomotors for detecting and removing heavy metal ions, Adv. Funct. Mater. 31 (21) (2021) 2010694.
[12] C. Li, Y. Yu, L. Wang, S. Zhang, J. Liu, J. Zhang, A.-B. Xu, Z. Wu, J. Tong, S. Wang, et al., A step-by-step strategy for controlled preparations of complex heterostructured colloids, Chem. Mater. 31 (22) (2019) 9513–9521.
[13] J. Liu, J. Li, G. Wang, W. Yang, J. Yang, Y. Liu, Bioinspired zeolitic imidazolate framework (zif-8) magnetic micromotors for highly efficient removal of organic pollutants from water, Journal of colloid and interface science 555 (2019) 234–244.
[14] H. Ye, Y. Wang, X. Liu, D. Xu, H. Yuan, H. Sun, S. Wang, X. Ma, Magnetically steerable iron oxides-manganese dioxide core–shell micromotors for organic and microplastic removals, J. Colloid Interface Sci. 588 (2021) 510–521.
[15] H.R. Vutukuri, M. Lisicki, E. Lauga, J. Vermant, Light-switchable propulsion of active particles with reversible interactions, Nature communications 11 (1) (2020) 1–9.
[16] S. Yuan, X. Lin, Q. He, Reconfigurable assembly of colloidal motors towards interactive soft materials and systems, J. Colloid Interface Sci. 612 (2022) 43–56.
[17] M.C. Marchetti, J.F. Joanny, S. Ramaswamy, T.B. Liverpool, J. Prost, M. Rao, R.A. Simha, Hydrodynamics of soft active matter, Reviews of modern physics 85 (3) (2013) 1143–1189.
[18] B.P. Kumar, A.J. Patil, S. Mann, Enzyme-powered motility in buoyant organoclay/dna protocells, Nature chemistry 10 (11) (2018) 1154–1163.
[19] F. Peng, Y. Men, Y. Tu, Y. Chen, D.A. Wilson, Nanomotor-based strategy for enhanced penetration across vasculature model, Adv. Funct. Mater. 28 (25) (2018) 1706117.
[20] Z. Xiao, M. Wei, W. Wang, A review of micromotors in confinements: Pores, channels, grooves, steps, interfaces, chains, and swimming in the bulk, ACS applied materials & interfaces 11 (7) (2018) 6667–6684.
[21] Y. Yang, X. Arque, T. Patin o, V. Guillerm, P.-R. Blersch, J. Perez-Carvajal, I. Imaz, D. Maspoch, S. Sanchez, Enzyme-powered porous micromotors built from a hierarchical micro-and mesoporous uio-type metal–organic framework, Journal of the American Chemical Society.
[22] A. Terzopoulou, J.D. Nicholas, X.-Z. Chen, B.J. Nelson, S. Pané, J. Puigmartí-Luis, Metal–organic frameworks in motion, Chem. Rev. 120 (20) (2020) 11175–11193.
[23] S. Sanchez, A.A. Solovev, Y. Mei, O.G. Schmidt, Dynamics of biocatalytic microengines mediated by variable friction control, J. Am. Chem. Soc. 132 (38) (2010) 13144–13145.
[24] L. Zhu, L. Zong, X. Wu, M. Li, H. Wang, J. You, C. Li, Shapeable fibrous aerogels of metal–organic-frameworks templated with nanocellulose for rapid and large-capacity adsorption, ACS nano 12 (5) (2018) 4462–4468.
[25] H. Ning, Y. Zhang, H. Zhu, A. Ingham, G. Huang, Y. Mei, A.A. Solovev, Geometry design, principles and assembly of micromotors, Micromachines 9 (2) (2018) 75.
[26] D.A. Edwards, J. Hanes, G. Caponetti, J. Hrkach, A. Ben-Jebria, M.L. Eskew, J. Mintzes, D. Deaver, N. Lotan, R. Langer, Large porous particles for pulmonary drug delivery, Science 276 (5320) (1997) 1868–1872.
[27] J. Song, F. Babayekhorasani, P.T. Spicer, Soft bacterial cellulose microcapsules with adaptable shapes, Biomacromolecules 20 (12) (2019) 4437–4446.
[28] Z. Guo, T. Wang, A. Rawal, J. Hou, Z. Cao, H. Zhang, J. Xu, Z. Gu, V. Chen, K. Liang, Biocatalytic self-propelled submarine-like metal-organic framework microparticles with ph-triggered buoyancy control for directional vertical motion, Mater. Today 28 (2019) 10–16.

[29] D. Saidane, E. Perrin, F. Cherhal, F. Guellec, I. Capron, Some modification of cellulose nanocrystals for functional pickering emulsions, Philosophical Transactions of the Royal Society A: Mathematical, Physical and Engineering Sciences 374 (2072) (2016) 20150139.
[30] D. Lahiri, M. Nag, B. Dutta, A. Dey, T. Sarkar, S. Pati, H.A. Edinur, Z. Abdul Kari, N.H. Mohd Noor, R.R. Ray, Bacterial cellulose: Production, characterization, and application as antimicrobial agent, Int. J. Mol. Sci. 22 (23) (2021) 12984.
[31] X. Ma, Y. Lou, X.-B. Chen, Z. Shi, Y. Xu, Multifunctional flexible composite aerogels constructed through in-situ growth of metal-organic framework nanoparticles on bacterial cellulose, Chem. Eng. J. 356 (2019) 227–235.
[32] J. Sun, M. Mathesh, W. Li, D.A. Wilson, Enzyme-powered nanomotors with controlled size for biomedical applications, ACS nano 13 (9) (2019) 10191–10200.
[33] C. He, K. Lu, W. Lin, Nanoscale metal–organic frameworks for real-time intracellular ph sensing in live cells, J. Am. Chem. Soc. 136 (35) (2014) 12253–12256.
[34] M. Mohammad, A. Razmjou, K. Liang, M. Asadnia, V. Chen, Metal–organic-framework-based enzymatic microfluidic biosensor via surface patterning and biomineralization, ACS applied materials & interfaces 11 (2) (2018) 1807–1820.
[35] R.M. Macnab, D.E. Koshland, The gradient-sensing mechanism in bacterial chemotaxis, Proc. Nat. Acad. Sci. 69 (9) (1972) 2509–2512.
[36] J. Schindelin, I. Arganda-Carreras, E. Frise, V. Kaynig, M. Longair, T. Pietzsch, S. Preibisch, C. Rueden, S. Saalfeld, B. Schmid, J.Y. Tinevez, D.J. White, V. Hartenstein, K. Eliceiri, P. Tomancak, A. Cardona, Fiji: An open-source platform for biological-image analysis, Nature Methods 9 (7) (2012) 676–682. arXiv:1081–8693, doi:10.1038/nmeth.2019.
[37] K.-Y. Lee, J.J. Blaker, A. Bismarck, Surface functionalisation of bacterial cellulose as the route to produce green polylactide nanocomposites with improved properties, Compos. Sci. Technol. 69 (15–16) (2009) 2724–2733.
[38] K. Liang, R. Ricco, C.M. Doherty, M.J. Styles, S. Bell, N. Kirby, S. Mudie, D. Haylock, A.J. Hill, C.J. Doonan, et al., Biomimetic mineralization of metal-organic frameworks as protective coatings for biomacromolecules, Nature communications 6 (1) (2015) 1–8.
[39] Y. Chen, V. Lykourinou, C. Vetromile, T. Hoang, L.-J. Ming, R.W. Larsen, S. Ma, How can proteins enter the interior of a mof? investigation of cytochrome c translocation into a mof consisting of mesoporous cages with microporous windows, J. Am. Chem. Soc. 134 (32) (2012) 13188–13191.
[40] J. Liang, K. Liang, Biocatalytic metal–organic frameworks: prospects beyond bioprotective porous matrices, Adv. Funct. Mater. 30 (27) (2020) 2001648.
[41] T. Patin o, X. Arque, R. Mestre, L. Palacios, S. Sanchez, Fundamental aspects of enzyme-powered micro-and nanoswimmers, Accounts of chemical research 51 (11) (2018) 2662–2671.
[42] W. Liang, H. Xu, F. Carraro, N.K. Maddigan, Q. Li, S.G. Bell, D.M. Huang, A. Tarzia, M.B. Solomon, H. Amenitsch, et al., Enhanced activity of enzymes encapsulated in hydrophilic metal–organic frameworks, J. Am. Chem. Soc. 141 (6) (2019) 2348–2355.
[43] M.M. Bradford, A rapid and sensitive method for the quantitation of microgram quantities of protein utilizing the principle of protein-dye binding, Analytical biochemistry 72 (1–2) (1976) 248–254.
[44] T. Patin o, N. Feiner-Gracia, X. Arque, A. Miguel-Lopez, A. Jannasch, T. Stumpp, E. Schaffer, L. Albertazzi, S. Sanchez, Influence of enzyme quantity and distribution on the self-propulsion of non-janus urease-powered micromotors, Journal of the American Chemical Society 140 (25) (2018) 7896–7903.
[45] J.K. Armstrong, R.B. Wenby, H.J. Meiselman, T.C. Fisher, The hydrodynamic radii of macromolecules and their effect on red blood cell aggregation, Biophysical journal 87 (6) (2004) 4259–4270.
[46] N. Carpita, D. Sabularse, D. Montezinos, D.P. Delmer, Determination of the pore size of cell walls of living plant cells, Science 205 (4411) (1979) 1144–1147.
[47] M. Rabe, D. Verdes, S. Seeger, Understanding protein adsorption phenomena at solid surfaces, Advances in colloid and interface science 162 (1–2) (2011) 87–106.
[48] M. Van der Zon, P. Hamersma, E. Poels, A. Bliek, Gas–solid adhesion and solid–solid agglomeration of carbon supported catalysts in three phase slurry reactors, Catal. Today 48 (1–4) (1999) 131–138.
[49] H. Vinke, P. Hamersma, J. Fortuin, Particle-to-bubble adhesion in gas/liquid/solid slurries, AIChE J. 37 (12) (1991) 1801–1809.